Journal of Materials Chemistry A

ROYAL SOCIETY OF CHEMISTRY

COMMUNICATION

View Article Online
View Journal | View Issue

Cite this: J. Mater. Chem. A, 2024, 12, 7508

Received 4th December 2023
Accepted 26th February 2024

DOI: 10.1039/d3ta07490k

rsc.li/materials-a

Novel heat storage ionomer binder for thermal management of Li-ion batteries†

Danni Shen,[a] Tingting Han,[e] Jie Liu, *[b] Junwu Yang,[e] Jinqiu Zhou,[b] Yufei Li,[d] Xi Zhou,[bf] Zhenkang Wang,[a] Tao Qian[b] and Chenglin Yan *[acf]

Lithium-ion batteries (LIBs) are promising for power batteries because of their high energy density and working voltage, but the high accident rate caused by the flammable electrolyte and constantly accumulating heat scares consumers and restricts their market. Herein, a novel heat storage ionomer binder (HSIB) with highly efficient heat-storage ability is proposed to function as an internal temperature conditioner, which can effectively store heat and accommodate temperature rise, allowing the battery to function steadily over a wider temperature range while not significantly increasing the weight or volume of the battery. A nail test and thermal simulation demonstrate that HSIB can decrease the temperature rise of the cell by about 30% and reduce the risk of thermal runaway due to the heat storage ability of the polyethylene glycol (PEG) main body. The assembled $LiFePO_4$ (LFP) cell with HSIB shows lower polarization (ΔV decreased by 25 mV over PVDF) in a CV test owing to fast Li^+ diffusion pathways constructed by the binder, and extra capacity and higher capacity retention of 14.38% are achieved. Moreover, an LFP cell with HSIB shows good thermal endurance in a designed temperature variation test, suggesting that HSIB offers a novel practical solution for battery safety.

1. Introduction

Ascribed to its various merits, such as high energy density, long cycle life, high working voltage, and low self-discharge rate, lithium-ion batteries (LIBs) have been applied in a vast number of applications, especially in the domains of portable electronics, smart grids, and vehicles;[1,2] however, they still confront various obstacles, among which safety is the most severe. Over decades, many events of spontaneous combustion and explosion induced by LIBs have been reported, which is becoming an increasing concern to governments, enterprises, and groups.[3] What makes LIBs more accident-prone are the deposition of highly reactive lithium metal on the electrode surface, sharp lithium dendrites, an organic carbonate electrolyte and higher energy density.[4,5] Additionally, explosion/combustion accidents with LIBs occur more quickly and powerfully, and the flame is difficult to extinguish, which can seriously endanger property, the environment and personal safety. Therefore, the safety of LIBs is a thorny but urgent problem to be solved.

In terms of mechanism, a great deal of heat can be released during the charge/discharge process of cells, and the heat dissipation rate will be less than the heat generation rate if the battery suffers severely abusive conditions (*i.e.* heat, electrical or mechanical abuse).[6,7] After that, thermal runaway (TR) is likely to be triggered due to the rise in temperature resulting from persistently accumulating heat. No matter what abusive conditions apply to LIBs, the trigger for TR must be a temperature-reaction-heat loop.[6] Therefore, heat abuse is necessary for TR. Specifically, mechanical abuse such as collisions and punctures can lead to poor contact or even short circuits, resulting in unhealthy lithium deposition or violent electrochemical reactions (electrical abuse). The electrical abuse process generates a large amount of heat, which increases the temperature of the battery (thermal abuse). The high temperature will accelerate the electrochemical reaction, induce side reactions, and damage the separator to a certain extent. In this process, the battery continues to self-heat because the heat production rate is greater than the cooling rate. Based on above points, inhibiting the self-heating of the battery, automatically cutting-off the electrochemical reaction, and improving the mechanical strength of the separator are effective ways to avoid TR. To improve the safety of batteries, strategies such as external cooling, solid

[a]College of Energy, Soochow University, Suzhou 215006, China. E-mail: c.yan@suda.edu.cn
[b]College of Chemistry and Chemical Engineering, Nantong University, Seyuan 9, Nantong 226019, China. E-mail: jliu93@ntu.edu.cn
[c]School of Petrochemical Engineering, Changzhou University, Changzhou 213164, China
[d]Pinghu Institute of Advanced Materials, Zhejiang University of Technology, Pinghu 314200, China
[e]State Key Laboratory of Space Power-Sources Technology, Shanghai Institute of Space Power-Sources, 2965 Dongchuan Road, Shanghai 200245, China
[f]Key Laboratory of Core Technology of High Specific Energy Battery and Key Materials for Petroleum and Chemical Industry, Soochow University, Suzhou, 215123, China

† Electronic supplementary information (ESI) available. See DOI: https://doi.org/10.1039/d3ta07490k

electrolytes, coatings, and electrolyte additives have been proposed.[8–10] Some of them can mitigate internal short circuits and side reactions, but often at the expense of battery performance, while they may not be effective for all thermal runaway routes.[11,12] Although the external cooling strategy can reduce the possibility of TR by inhibiting the temperature-reaction-heat loop, it fails on timely reduction of the core temperature of the cell, but causes a temperature difference and occupies a certain volume of the equipment. If the generated heat can be absorbed inside the cell, the internal temperature of the cell can be reduced in a more timely and even manner.[13] Consequently, not only can the probability of TR be reduced but the side reactions at higher temperature can also be suppressed.

Phase-change materials have the characteristics of absorbing/releasing a large amount of latent heat during the phase-change process, which can maintain the ambient temperature at a suitable level, therefore, they are widely used in construction, as well as in the external thermal management of batteries.[14] Herein, we creatively report a heat storage ionomer binder (HSIB) with the function of heat storage. On the one hand, it can effectively store heat, thereby reducing the maximum temperature of the battery, which can delay or even avoid TR. On the other hand, due to its replacement of a traditional binder, HSIB is able to uniformly adjust the cell temperature and retain a higher degree of battery performance under mild heat abuse conditions, without increasing the volume or weight of the device. The binder takes polyethylene glycol (PEG) as a heat storage component and tannic acid (TA) to form hydrogen bonds and is finally formed by cross-linking iron ions.[15] The hydrogen bond between PEG and TA provides good cohesion, and the coordinated bond between TA molecules further improves its structural stability. HSIB not only inherits the phase-change properties of PEG but also promotes fast Li^+ diffusion kinetics by a couple/decouple reaction between Li^+ and the O of C=O and C–O.[16–18] A nail test and thermal simulation demonstrate that HSIB is able to dramatically lower the self-heating rate of the battery by about 30% by storing the reaction heat and ohmic heat of electrochemical processes. The results of cycling tests at room temperature and variable temperature show that assembled Li||$LiFePO_4$ (LFP) cells with this ionomer binder exhibit superior electrochemical performance (an increase of more than 14% in capacity retention) and heat resistance. Therefore, HSIB can simultaneously improve the electrochemical performance, thermal endurance and safety of the battery, without sacrificing the energy density, which has great significance for innovative material research and novel thermal management solutions in the energy field.

2. Results and discussion

2.1 Design and fabrication of HSIB

The heat storage ionomer binder was synthesized to absorb and release the latent heat from temperature difference, ohm heat and reaction heat when the battery is working (Fig. 1(a)), further

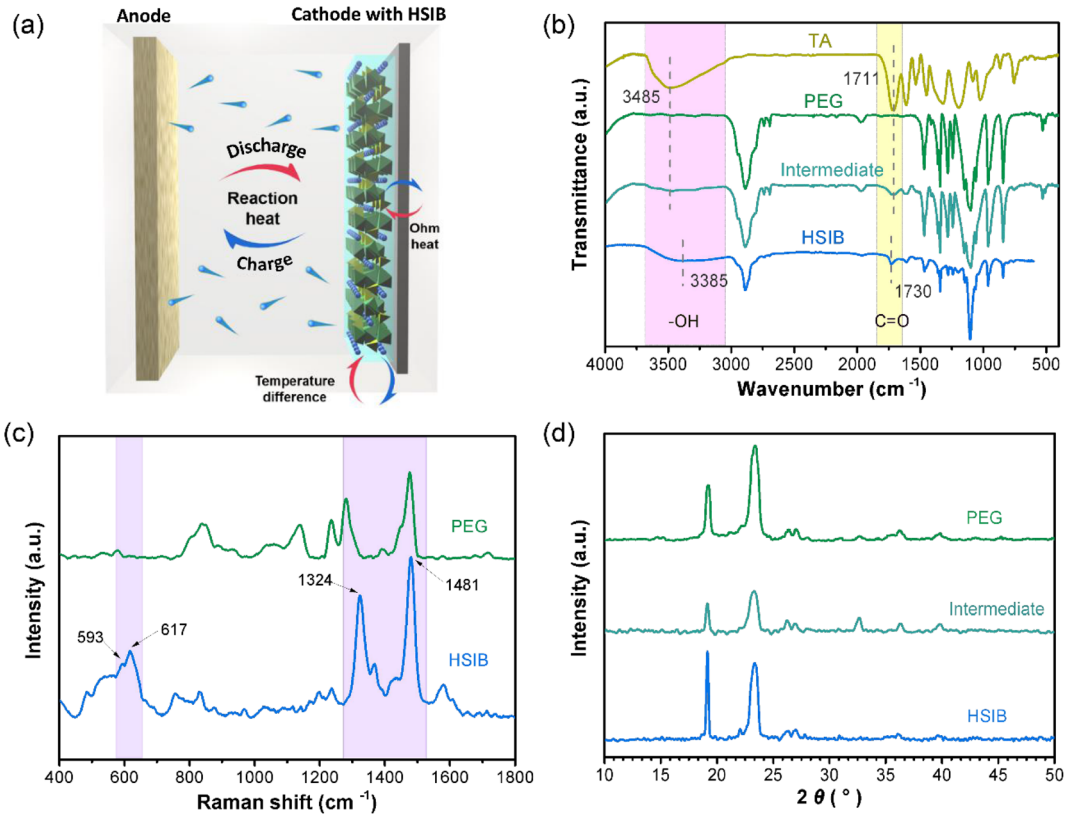

Fig. 1 (a) Schematic diagram of the heat storage process for an LFP cell with HSIB. (b) FTIR spectra, (c) Raman spectra and (d) XRD patterns of different samples.

alleviating the adverse effects of heat on the battery. HSIB is formed *via* numerous hydrogen bonds and coordinate bonds (Fig. S1†). Specifically, TA is hydrogen-bonded to PEG molecules, providing extra C=O and C–O that can be coupled/uncoupled with Li^+,[18] while Fe^{3+} is further chelated with TA catechol to form a robust polymer network.

To confirm the existence of hydrogen bonds in HSIB, Fourier transform infrared reflection (FTIR) spectra were utilized to detect differences in relevant functional groups between PEG, TA, the intermediate (which is without the coordinate bonds of Fe^{3+}) and HSIB (Fig. 1(b)). The formation of hydrogen bonds affects the vibrational frequencies of hydroxyl (–OH) and carbonyl (C=O), shifting vibrational peaks to low and high wavenumbers accordingly.[19] Due to the ample O and H elements of TA, the force of the hydrogen bond is intrinsic, which pushes the –OH peak and C=O peak of HSIB to shift from 3485 cm^{-1} to 3385 cm^{-1} and from 1711 cm^{-1} to 1730 cm^{-1}, respectively. The constraint of plenty of hydrogen bonds weakens the vibrational energy of –OH, decreasing the wavenumber of the –OH stretch vibration. The increase in wavenumber for the C=O stretch vibration is ascribed to the strengthened vibrational energy of C=O because of the interaction with the hydrogen donor.[15] The formation of Fe–O coordinate bonds was further proved by Raman spectra. The peaks around 593 cm^{-1}, 617 cm^{-1}, 1324 cm^{-1} and 1481 cm^{-1} in Fig. 1(c) show that Fe^{3+} interacts with the –OH of the substituted catechol groups of TA.[15,20,21] X-ray diffraction (XRD) was measured to display the difference in the crystalline structure of HSIB and dominant component PEG. As shown in Fig. 1(d), after the addition of TA, the prominent diffraction peaks of PEG which are located at 18.6°–19.8° and 22.4°–24.1° are significantly weakened. This suggests that the intermediate has lower crystallinity.[22,23] However, after reacting with Fe^{3+}, the intensities of these two peaks are greatly enhanced, and their ratio is inversely changed compared with the intermediate and PEG. The changed intensity ratio implies that HSIB has a slight preferred orientation.[24–26] This result indicates that the lattice of PEG is greatly changed by the effect of the hydrogen bonds and coordinate bonds attributed to TA and Fe^{3+}.

2.2 Thermal management capability of HSIB

The thermal property of HSIB was explored by *in situ* XRD and differential scanning calorimetry (DSC), as shown in Fig. 2(a) and (b). HSIB absorbs heat and undergoes a phase transition from crystalline to amorphous with rising temperature, resulting in significant phase-change enthalpy and transformation of the XRD pattern. To confirm the significant phase transition ability of HSIB after preparation of the electrode, the material was scraped off the electrode and characterized by DSC (Fig. 2(c)). The HSIB cathode shows a prominent endothermic peak in the range of 50 to 70 °C, implying significant heat storage capacity.

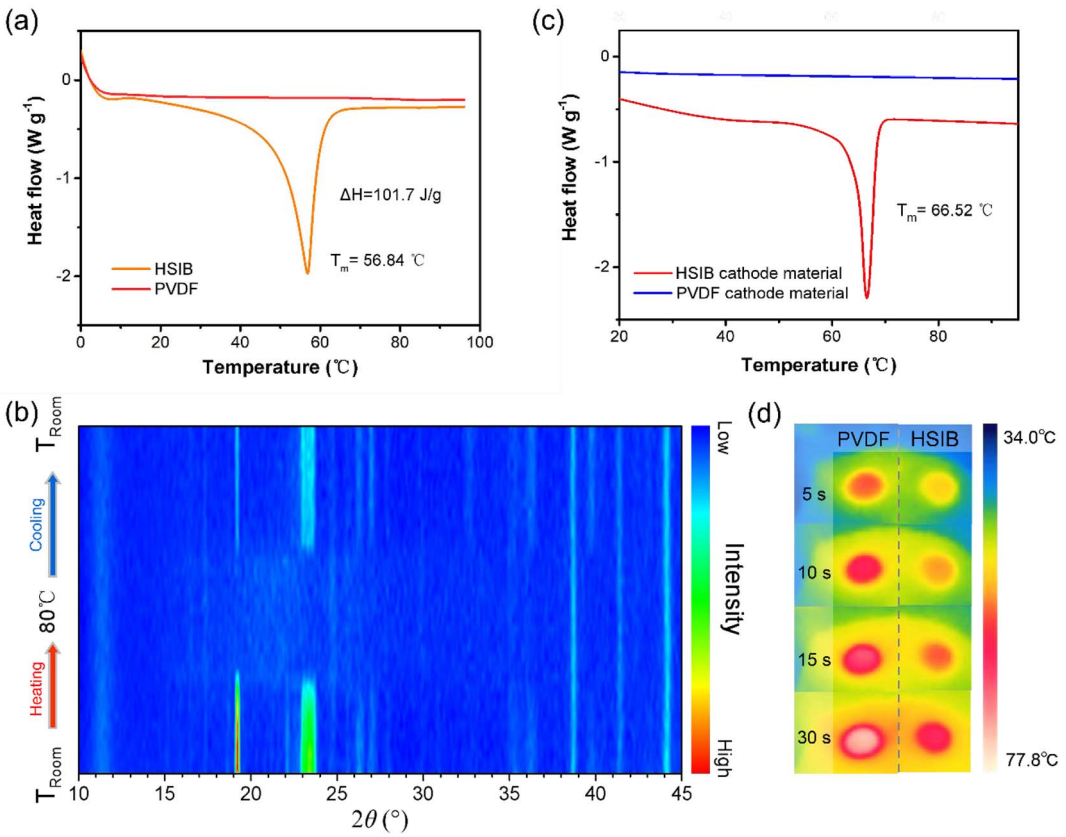

Fig. 2 (a) DSC curves of PVDF and HSIB samples. (b) *In situ* XRD pattern of HSIB under continuous temperature-rising and temperature-reducing conditions. (c) DSC curves of different cathodes. (d) Thermal imaging images of cathodes heated by infrared lamp.

In contrast, the DSC curve of a PVDF (polyvinylidene fluoride) cathode exhibits negligible change with rising temperature. The heat storage ability of the electrodes was displayed by thermal images. To heat the electrodes, an infrared lamp was employed to heat cathodes slowly and simultaneously, and the heating conditions of samples were controlled to be the same. It is obviously that the HSIB cathode is closer to room temperature (T_{room}) when heated under same conditions (Fig. 2(d)).

Thermal simulation and a nail test were conducted to reflect the thermal management performance of HSIB under conditions of severe temperature rise during thermal runaway and slow temperature rise during daily use. For the thermal simulation, a model of a unit cell of an LFP pouch cell was constructed (Fig. 3(a)), and the parameters of the 3D model are shown in Table S1.† To fully reflect the heating and cooling rate of the pouch cell, a charge–discharge cycle was adopted in an adiabatic environment followed by sufficient natural convection cooling. After 70 min of charge/discharge simulation (7 cycles in 4 C) with heat isolation and natural cooling for 1 min, the core temperatures of PVDF and HSIB pouch cell models were 101.26 °C and 76.29 °C, respectively (as shown in Fig. 3(b)). It is exciting that HSIB could lead to a suppressed temperature rise of about 36% (as shown in Table S2†) compared to the contrast sample.

To simulate the practical effect of HSIB on controlling the temperature rise of batteries, nail-penetration experiments were conducted on the pouch cells. The A h-level LFP||graphite pouch cells were pre-charged to 200 mA h to control the maximum temperature of the cell after penetration. In an empty and windless environment, we placed the pouch cell on a thick foam board and pierced it with a hammer and an awl to a maximum diameter

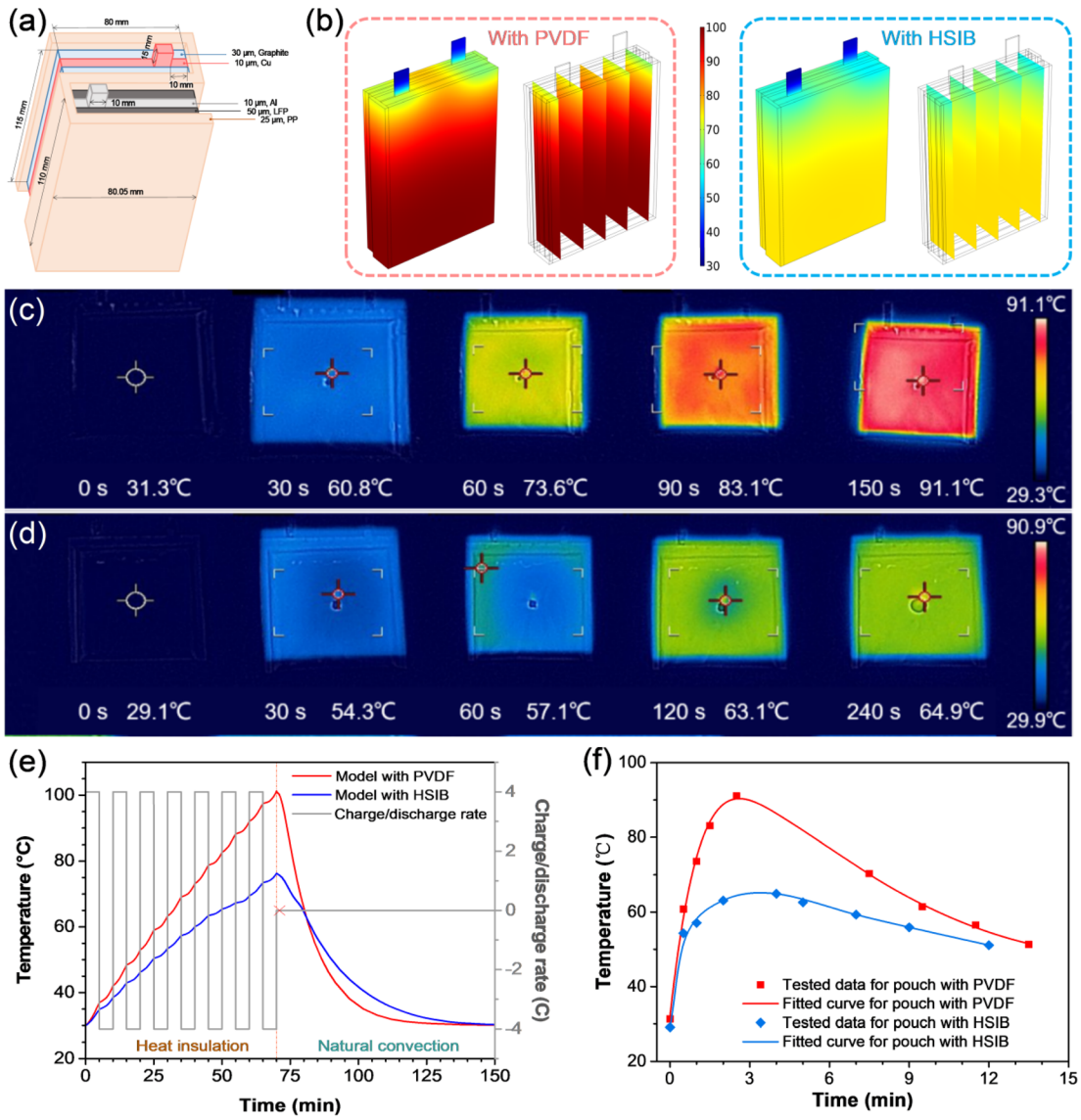

Fig. 3 (a) Diagram of unit cell structure for thermal simulation. (b) Comparison of temperature distribution in the thermal simulation of a 2 A h LFP pouch cell based on charge/discharge cycles in 4 C area current density (48 A m^{-2}). Heating process of the LFP pouch cell with (c) PVDF and (d) HSIB after nailing. (e) Variation in temperature and current density by time in the thermal simulation process. (f) Change in the maximum temperature with time after the pouch cells were penetrated.

of 5 mm. The temperature change of the pouch cells during the nail test was detected by an infrared camera and is plotted in Fig. 3(c), (d) and S2.† The maximum temperature of the pouch cell with HSIB is 64.9 °C, while that with a PVDF binder is 91.1 °C, delivering a total reduction of 25.2 °C. Moreover, the temperature change of the pouch cell with HSIB is slower than that of the cell with a PVDF binder, whether in the rapid heating process after nailing or during the cooling process from 60 °C to 50 °C.

The results of the nail test and thermal simulation are similar. The trend in temperature changes in the simulation is drawn in Fig. 3(e) for a distinctive comparison, and the maximum cell temperature after penetration is plotted in Fig. 3(f). At the 60th min, the core temperature of the model for HSIB is 69.55 °C while that for the PVDF model is 92.1 °C; for the nail test, they are 64.9 °C and 91.1 °C, respectively. Both show a significant plateau in temperature change (for thermal simulation, it is between the 45th and 60th min for the temperature curve of the HSIB model, corresponding to a range of 63.44 °C to 69.55 °C) corresponding to the endothermic peak of the DSC curve of the HSIB cathode. As a trigger point for TR, SEI decomposition occurs above 70 °C.[27] Thus, the HSIB electrode with a phase-transition temperature below 70 °C, can not only suppress the temperature rise by absorbing existing heat, but it can also avoid violent side reactions and subsequent TR. Besides, HSIB shows a slower heating/cooling rate in thermal simulation and nail test, indicating its ability to avoid drastic changes in temperature. According to the thermal performance characterization mentioned above, HSIB can significantly reduce safety risks and damage to battery performance by suppressing temperature fluctuations and limiting the maximum temperature that the battery can reach.[28]

2.3 Electrochemical performance

A cyclic voltammetry (CV) test was employed for the primary determination of the electrochemical performance of the resulting coin half-cell, such as redox potential, capacity, and electrode-reaction reversibility. The ideal CV curve for the coin

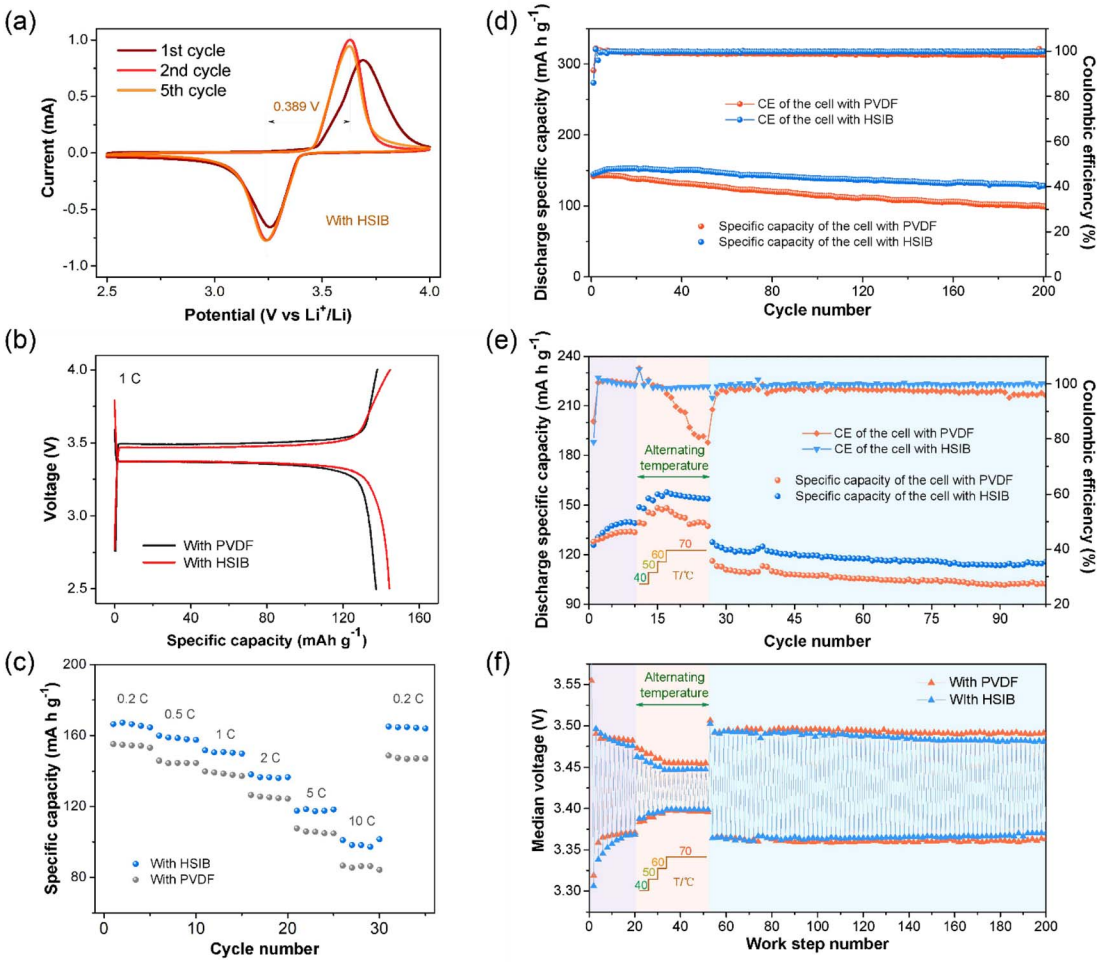

Fig. 4 (a) CV curves for LFP||Li half cells with HSIB cathode; the sweep rate is 0.5 mV s^{-1}. (b) Charge/discharge curves of the half-cells with PVDF and HSIB in 1 C (170 mA g^{-1}). (c) Rate performance of LFP||Li cells based on an HSIB cathode and a PVDF cathode under different current densities. (d) Cycle performance of the cells with PVDF and HSIB. (e) Cycle performance of the half-cells in a temperature variation test at 1 C. The orange region indicates the variable temperature condition from T_{room} to 70 °C as marked in the plot, and the cycles in purple and blue regions are run at T_{room} before and after temperature alternation, respectively. (f) Median voltage of charge/discharge steps in a temperature variation test to indicate the polarization of the cells.

cell with HSIB is depicted in Fig. 4(a), which shows that HSIB does not obstruct the redox reaction. Additionally, the redox peak spacing of the cell with HSIB is closer (0.389 V) than that with PVDF (0.414 V) (Fig. S3(a)†), demonstrating that the cell with HSIB experiences less polarization. Based on virtually overlapping 2nd and 5th curves, the electrode exhibits strong redox reversibility. In contrast, the CV curves of the cell with PEG (which is without the limitations of hydrogen bonds and coordinate bonds) display several redox peaks that fail to greatly overlap, which are caused by the disordered electrode reaction (Fig. S3(b)†). The charge/discharge curves (Fig. 4(b)) also reflect that the cell with HSIB has lower resistance and polarization than that with PVDF. To explore the ionic conductivity of HSIB, we added $LiPF_6$ as an Li source to molten HSIB to assemble a stainless-steel symmetric cell. As shown in Fig. S4,† 1 M $LiPF_6$ in pure HSIB delivers high ionic conductivity ranging from 10^{-6} S cm^{-1} to 10^{-3} S cm^{-1} at temperatures between 25 °C and 130 °C, which approaches that of an ordinary solid electrolyte[17,29–31] and is higher than that of PVDF.[32,33] For the rate test, the capacities of the cell with HSIB in 0.2 C, 0.5 C, 1 C, 2 C 5 C and 10 C are 166.4, 158.3, 150.4, 136.4, 117.9 and 98.2 mA h g^{-1} respectively, significantly higher than for the PVDF cathode (Fig. 4(c)). The cell with an HSIB cathode performs with a high capacity of 152.9 mA h g^{-1} and good cycle stability at 1 C (Fig. 4(d)). An EIS test after cycles was also executed. As shown in Fig. S5,† the arc part of impedance curves could be divided into two smaller arcs, which represent the Li^+ diffusion impedance in SEI (R_{SEI}) and charge transfer impedance at the conductive junction (R_{ct}), respectively. The R_{ct} arc of the cell with HSIB gradually shrinks over cycles, implying reduced charge transfer impedance. In contrast, the R_{ct} and R_{SEI} of the half-cell with PVDF obviously increased over a long period of charge/discharge, indicating the growth and passivation of SEI. The bulk resistance (R_b) of the cell with HSIB declines as well, which is attributed to the enhanced ionic conductivity that resulted from the ion transport pathways constructed by the C=O and C–O of HSIB.[18] The results of the equivalent circuit fitting are listed in Table S3.† The lowered polarization and reduction in charge-transfer resistance after activation are inferred to be the result of role of HSIB in Li^+ transmission and storage, which is realized by the coupling and decoupling reaction of Li^+ and O of hydroxyl and the ester group.[17,34] The coordination-type conductive HSIB reduces the surface adsorption free energy at the interface, which is conducive to the transfer of Li^+ from the cathode to the interface[16] and is beneficial to the relaxation of the Li^+ concentration gradient.[35] Consequently, enhanced electrode kinetics bestow higher capacity upon the cell with HSIB.

A temperature alternation test was designed to explore the thermal endurance of the cells in this work. As shown in Fig. 4(e) and (f), the LFP half-cells with an HSIB cathode and a PVDF cathode are similar in performance in the 5–10th cycles after the initial activation process. In the following single cycle temperature alternation process, it is hard to judge the thermal effect of HSIB from the cell voltage (Fig. S6†). However, in subsequent cycles, the widening difference in the specific capacity and polarization (indicated by the median voltage) of the two batteries means that the cell with HSIB has better heat endurance. For cycles at 70 °C, it is clearly shown that the cell with PVDF has been irreversibly damaged by the high temperature, resulting in the stubborn enlarged polarization and capacity loss. The performance degradation of the cells at 70 °C can reasonably be attributed to the side reaction of trace water in the electrolyte with $LiPF_6$ and the side reaction of SEI decomposition. For HSIB, its heat storage function makes the cell reach the SEI decomposition temperature later, further lowering the degree of SEI side reaction. Though the coulombic efficient (CE) of the cell with PVDF is basically returned when the hot environment is removed, it constantly declined with ongoing cycles. For which with HSIB, no CE decay was observed, and the amplified polarization decreased with cycling. This phenomenon may be attributed to the fact that the breaking/regeneration of hydrogen bonds and coordination bonds can align particles and thus promote their close packing. Moreover, the Li anode of the cell with HSIB after the temperature alternation test shows a better appearance, and the cathode still sticks to Al foil without any peeling or dissolution, implying the physical and electrochemical stability of the HSIB cathode and good thermal endurance of the resulting cell (Fig. S7†).

3. Conclusions

HSIB, a novel binder for LIB with a temperature regulation function, was designed and probed. It has a suitable phase-transition temperature and enthalpy and shows a remarkable heat storage effect at the material level and enables a 28% to 36% temperature decrease in the LFP cell in a simulation. As a result, HSIB is capable of smoothing temperature fluctuation during normal operation and greatly reduces the risk of thermal runaway. Moreover, the resulting HSIB cathode is electrochemically stable for an LFP coin cell. Benefiting from the synergistic effect of plenty of hydrogen bonds and coordinate bonds and ion transfer pathways of C=O and C–O, side reactions of PEG and the negative effect of high temperature are limited, leading to an ideal CV curve, good rate performance and temperature tolerance for HSIB. Our study provides a novel method for battery safety, increases the possibility of more functional binders, and broadens the application prospects of LIBs.

4. Experimental section

See experimental details in the ESI.†

Conflicts of interest

The authors declare no conflict of interest.

Acknowledgements

This work was supported by the National Natural Science Foundations of China (No. U21A20332, 52071226, and 52002190) and the Project of Key Laboratory of Core Technology

of High Specific Energy Battery and Key Materials for Petroleum and Chemical Industry, Soochow University (No. SDHY2241).

References

1 J. Liu, Y. Cao, J. Zhou, M. Wang, H. Chen, T. Yang, Y. Sun, T. Qian and C. Yan, *ACS Appl. Mater. Interfaces*, 2020, **12**, 54537–54544.
2 L. Wang, Y. Zhang and P. G. Bruce, *Natl. Sci. Rev.*, 2023, **10**, nwac062.
3 Z. Liu, Q. Hu, S. Guo, L. Yu and X. Hu, *Adv. Mater.*, 2021, **33**, e2008088.
4 X. Feng, M. Ouyang, X. Liu, L. Lu, Y. Xia and X. He, *Energy Storage Mater.*, 2018, **10**, 246–267.
5 R. C. Massé, C. Liu, Y. Li, L. Mai and G. Cao, *Natl. Sci. Rev.*, 2017, **4**, 26–53.
6 J. Liu, J. Zhou, M. Wang, C. Niu, T. Qian and C. Yan, *J. Mater. Chem. A*, 2019, **7**, 24477–24485.
7 J. Wang, K. Yang, S. Sun, Q. Ma, G. Yi, X. Chen, Z. Wang, W. Yan, X. Liu, Q. Cai and Y. Zhao, *InfoMat*, 2023, **5**, e12401.
8 R. Fan, N. Zheng and Z. Sun, *Int. J. Heat Mass Transfer*, 2021, **166**, 120753.
9 C. Xiao, G. Zhang, Z. Li and X. Yang, *J. Mater. Chem. A*, 2020, **8**, 14624–14633.
10 C. Y. Wang, G. Zhang, S. Ge, T. Xu, Y. Ji, X. G. Yang and Y. Leng, *Nature*, 2016, **529**, 515–518.
11 X. Liu, D. Ren, H. Hsu, X. Feng, G. Xu, M. Zhuang, H. Gao, L. Lu, X. Han, Z. Chu, J. Li, X. He, K. Amine and M. Ouyang, *Joule*, 2018, **2**, 2047–2064.
12 J. Hou, X. Feng, L. Wang, X. Liu, A. Ohma, L. Lu, D. Ren, W. Huang, Y. Li, M. Yi, Y. Wang, J. Ren, Z. Meng, Z. Chu, G.-L. Xu, K. Amine, X. He, H. Wang, Y. Nitta and M. Ouyang, *Energy Storage Mater.*, 2021, **39**, 395–402.
13 J. Gou, W. Liu and Y. Luo, *Appl. Therm. Eng.*, 2019, **161**, 114102.
14 M. M. Umair, Y. Zhang, K. Iqbal, S. Zhang and B. Tang, *Appl. Energy*, 2019, **235**, 846–873.
15 H. Fan, L. Wang, X. Feng, Y. Bu, D. Wu and Z. Jin, *Macromolecules*, 2017, **50**, 666–676.
16 C. H. Tsao, T. K. Yang, K. Y. Chen, C. E. Fang, M. Ueda, F. H. Richter, J. Janek, C. C. Chiu and P. L. Kuo, *ACS Appl. Mater. Interfaces*, 2021, **13**, 9846–9855.
17 Z. Li, J. Fu, X. Zhou, S. Gui, L. Wei, H. Yang, H. Li and X. Guo, *Adv. Sci.*, 2023, **10**, e2201718.
18 Z. Lin, X. Guo, Z. Wang, B. Wang, S. He, L. A. O'Dell, J. Huang, H. Li, H. Yu and L. Chen, *Nano Energy*, 2020, **73**, 104786.
19 K. H. Khoultchaev, P. Pang, R. J. Kerekes and P. Englezos, *Can. J. Chem. Eng.*, 1998, **76**, 261–266.
20 D. X. Oh, S. Kim, D. Lee and D. S. Hwang, *Acta Biomater.*, 2015, **20**, 104–112.
21 S. W. Taylor, D. B. Chase, M. H. Emptage, M. J. Nelson and J. H. Waite, *Inorg. Chem.*, 1996, **35**, 7572–7577.
22 C. C. Vidyasagar and Y. Arthoba Naik, *Arabian J. Chem.*, 2016, **9**, 507–510.
23 Y. Yuan, H. Zhang, N. Zhang, Q. Sun and X. Cao, *J. Therm. Anal. Calorim.*, 2016, **126**, 699–708.
24 S. Gao, W. Wei, M. Ma, J. Qi, J. Yang, S. Chu, J. Zhang and L. Guo, *RSC Adv.*, 2015, **5**, 51483–51488.
25 H. Li and W. Li, *Mater. Lett.*, 2022, **318**, 132227.
26 Z. Fang, N. Yan and S. Liu, *InfoMat*, 2022, **4**, e12369.
27 X. Tian, Y. Yi, B. Fang, P. Yang, T. Wang, P. Liu, L. Qu, M. Li and S. Zhang, *Chem. Mater.*, 2020, **32**, 9821–9848.
28 L. Kong, Y. Li and W. Feng, *Electrochem. Energy Rev.*, 2021, **4**, 633–679.
29 X. Zhu, Z. Fang, Q. Deng, Y. Zhou, X. Fu, L. Wu, W. Yan and Y. Yang, *ACS Sustainable Chem. Eng.*, 2022, **10**, 4173–4185.
30 L. Qiao, S. Rodriguez Pena, M. Martinez-Ibanez, A. Santiago, I. Aldalur, E. Lobato, E. Sanchez-Diez, Y. Zhang, H. Manzano, H. Zhu, M. Forsyth, M. Armand, J. Carrasco and H. Zhang, *J. Am. Chem. Soc.*, 2022, **144**, 9806–9816.
31 F. Zheng, H.-T. Li, Y.-Z. Zheng, D. Wang, N.-N. Yang, H.-Y. Ding and X. Tao, *Rare Met.*, 2022, **41**, 1889–1898.
32 S. Bi, C.-N. Sun, T. A. Zawodzinski Jr, F. Ren, J. K. Keum, S.-K. Ahn, D. Li and J. Chen, *J. Polym. Sci., Part B: Polym. Phys.*, 2015, **53**, 1450–1457.
33 Z. Zhang, D. Han, M. Xiao, S. Wang, Y. Feng, S. Huang and Y. Meng, *Ionics*, 2023, **29**, 3895–3906.
34 X. Wang, X. Shen, P. Zhang, A.-J. Zhou and J.-B. Zhao, *Rare Met.*, 2023, **42**, 875–884.
35 D. O. Shin, H. Kim, J. Choi, J. Y. Kim, S. H. Kang, Y. S. Park, M. Cho, Y. M. Lee, K. Cho and Y. G. Lee, *ACS Appl. Mater. Interfaces*, 2023, **15**, 13131–13143.

